Chemical Science

ROYAL SOCIETY OF CHEMISTRY

EDGE ARTICLE

View Article Online
View Journal | View Issue

Cite this: *Chem. Sci.*, 2024, **15**, 4938

All publication charges for this article have been paid for by the Royal Society of Chemistry

Covalent crosslinking chemistry for controlled modulation of nanometric roughness and surface free energy†

Debasmita Sarkar,‡[a] Manideepa Dhar,‡[a] Avijit Das,[a] Sohini Mandal,[a] Anirban Phukan[a] and Uttam Manna *[abc]

Smooth interfaces embedded with low surface free energy allow effortless sliding of beaded droplets of selected liquids—with homogeneous wettability. Such slippery interfaces display low or moderate contact angles, unlike other extremely liquid repellent interfaces (*e.g.* superhydrophobic). These slippery interfaces emerged as a promising alternative to extremely liquid repellent hierarchically rough interfaces that generally suffer from instability under severe conditions, scattering of visible light because of the hierarchically rough interface, entrapment of fine solid particulates in their micro-grooves and so on. However, a controlled and precise modulation of surface free energy and nanometric roughness is essential for designing a more compelling solid and dry antifouling interface. Here, we have unprecedentedly demonstrated the ability of covalent cross-linking chemistry for precise and simultaneous modulation of both essential surface free energy (~49 mN m^{-1} to ~22 mN m^{-1}) and roughness (root mean square roughness from 30 nm to 3 nm) of a solid interface for achieving liquid, substrate, and process independent, robust slippery properties. The strategic selection of β-amino-ester linkage through a 1,4-conjugated addition reaction between amine and acrylate groups of a three component reaction mixture (dominated by a 61% (w/w) crosslinker) under ambient conditions provided a facile basis for associating various important and relevant properties—including self-cleaning ability, anti-smudge properties (against both water and oil-based inks), thermal stability (>300 °C), chemical stability, physical durability, optical transparency (~95%) and so on. The embedded slippery properties of the coating remained unaffected at both low (0 °C) and high (100 °C) temperatures. Thus, the prepared coating would be appropriate to maintain the unperturbed performance of commercially available solar cell modules and other relevant objects under outdoor conditions.

Received 13th November 2023
Accepted 18th February 2024

DOI: 10.1039/d3sc06077b

rsc.li/chemical-science

Introduction

The growing concerns about the worldwide change in the climate and global energy crisis trigger the search for potential renewable power sources.[1–7] In this context, the outdoor installation of photovoltaic solar panels that convert sunlight into electrical energy emerged as one of the leading and promising approaches.[8–11] However, unavoidable deposition of different forms of particulate matter, such as dust, dirt, soot, fly ash, pollen, and other organic waste, under outdoor conditions appeared as an Achilles heel towards its unperturbed performance.[12–18] In fact, the deposition of fine dust particles that block exposure to sunlight reduces the efficiency of the solar panel by up to 50%.[13] While the limited efficiency of solar panels remained a concern towards energy production cost, the deposited dust would also substantially impact the cost of operation and maintenance of solar panels. To address this concern, various cleaning approaches—including manual cleaning, equipment-based brush cleaning, electrostatic cleaning, vibrating cleaning, heliotex cleaning, forced-air cleaning, *etc.*, were introduced in the literature.[12,13,19–23] While manual cleaning is time-consuming and laborious, equipment-based cleaning approaches demand complex construction and external power sources. Similarly, several other routinely used commercial goods made up of glass, wood, metal, *etc.*, suffer

[a]*Bio-Inspired Polymeric Materials Lab, Department of Chemistry, Indian Institute of Technology-Guwahati, Kamrup, Assam 781039, India. E-mail: umanna@iitg.ac.in*
[b]*Centre for Nanotechnology, Indian Institute of Technology Guwahati, Kamrup, Assam 781039, India*
[c]*Centre for Nanotechnology, School of Health Science and Technology, Indian Institute of Technology Guwahati, Kamrup, Assam 781039, India*

† Electronic supplementary information (ESI) available: Fig. S1–S22 depicting the detailed characterization of impact of cross-linker on the sol–gel conversion of the reaction mixture, progression of the reaction, FTIR characterization, impact of surface free energy of the coating, effect of different cross-linkers on the wettability, elemental mapping analysis for coatings, wettability of the coating for various liquids, different physical durability tests, anti-fouling performance of the coating, bright field microscopy images of different solid particulates, and coating on solar cell modules and different other substrates. See DOI: https://doi.org/10.1039/d3sc06077b

‡ These authors contributed equally to this work.

from unwanted and unavoidable fouling of liquids (aqueous and oil/oily contaminants)—causing inconvenience to keep these substrates clean and dry. Hence, further development is required to achieve a convenient and energy-efficient cleaning process for the cost-effective maintenance of solar panels and other widely used commercial goods.

In this context, inspired by the self-cleaning phenomenon of extremely water-repellent lotus leaves, many research groups have developed different artificial superhydrophobic coatings that displayed heterogeneous water wettability with a water contact angle of >150°, to demonstrate the removal of deposited dust particles by simply rolling beaded water droplets.[24–28] Even after significant progress on this research topic, it is still difficult to design an optically transparent and robust superhydrophobic coating that would be adequate for outdoor applications. The meta-stable trapped air present in the hierarchically featured interface (consisting of micro and nano-domains) that confers superhydrophobicity remains highly labile under abrasive and severe conditions—including scratching, extremes of temperature, high humidity, *etc.*[29–32] More importantly, porous/hierarchically featured superhydrophobic interfaces with empty groves and pores tend to

Table 1 The comparison of the prepared solid slippery coating with previous reports with respect to substrate independence, fabrication process, liquid repellency, optical transparency, thermal stability, and chemical durability

Selected substrates	Fabrication conditions	Ability to slide oils	Optical transparency	Thermal stability	Chemical durability	Ref. no.
Glass	Room temperature	No	92%	—	—	49
Polymer film	130 °C in a vacuum oven	No	—	—	NIR irradiation and silicone oil for 6 months	50
Glass	80 °C temperature	No	—	—	pH (1–13) for 40 h	51
ITO	Hydrothermal/80 °C	No	—	—	—	52
Glass, silicon, ceramics, metals, and plastics	100 °C temperature	Silicone oil	77.3%	60 °C	—	53
Glass	60 °C, 50 mbar	No	—	—	—	54
Glass and PET	75 °C	No	∼90%	100 °C	—	55
Silicon wafer and gold	Room temperature	No	—	—	—	56
Silicone wafer, glass, FTO, conductive glass, and metals	UV irradiation	No	—	—	1 M NaOH (10 min) NaCl solution (1 h)	57
Gold wafer	Room temperature	No	—	35 °C	—	58
Glass, silicon, and aluminium	60 °C temperature	Crude oil	∼92%	105 °C	—	60
Glass, silicon wafer, titanium dioxide, silicon oxide, and zinc oxide	Room temperature	Castor oil and seed oil	∼90%	70 °C	Sonication (45 kHz, 60 W) for 6 h in toluene	61
Glass, stainless steel, wood, and cotton fabric	120 °C temperature	No	90%	—	—	62
Glass and silicon wafer	Room temperature	No	90%	100 °C	UV irradiation (30 days) 100 °C (30 days)	63
Glass	120 °C temperature	Veg oil	≥92%	200 °C	pH 1 and pH 2 for 1 month pH 11 and pH 12 for 12 h	64
Glass and Al-plate	Room temperature	No	80.6%	240 °C	UV irradiation for 1 month Ambient conditions for 6 months	65
Glass and polymer films	80 °C temperature	No	97%	—	pH 1, pH 12, DTAB (1 mM), SDS (1 mM), seawater, river water, and UV (15 days)	66
Glass and PET	UV curing	No	98%	—	—	67
Glass, PTFE, Al, and Cu sheets	Melt casting	Grape seed oil and olive oil	—	90 °C	UV irradiation (30 days)	68
Glass, PET, and steel	UV curing	Pump oil, cooking oil, coal oil, and crude oil	>80%	100 °C	pH (2–13) for 12 h Organic solvent exposure for 72 h	69
Glass	150 °C temperature	No	95%	—	—	70
Glass, paper, metal, plastic, and wood	Room temperature, no additional treatment with UV light or elevated temperature	Krytox, vegetable oil, motor oil, crude oil, diesel, petrol, and kerosene	∼95%	300 °C	Exposure to pH 1, pH 12, DTAB (1 mM), SDS (1 mM), seawater, and river water for 15 days Exposure to UV (254 nm and 365 nm) for 1 month and ambient conditions for 6 months	This work

accumulate fine solid particulates and fail to self-clean the interface completely.[33] On the other side, superhydrophobic interfaces are readily fouled by the exposure of low surface tension liquids.[34] As an alternative approach, superamphiphobic interfaces were developed through the association of rough and specialized topography with environmentally toxic fluorinated modifications to prevent wetting by low surface tension liquids.[35–41] However, such interfaces would be inappropriate to self-clean fine particles as these rough interfaces are likely to trap any deposited fine particulate matter in their groves.[35] The only option to minimize the trapping of fine particles on solid surfaces is to prepare super liquid-repellent interfaces with low (below 500 nm) pore size.[33,42]

Hence, the design of a non-fluorinated ultra-smooth coating that displays homogeneous liquid wettability and effortlessly slides all types of liquids—including water, organic solvents, crude/refined/natural oils, and fluorinated liquid droplets, irrespective of the contact angle of the beaded liquid droplet, would be a promising alternative to achieve comprehensive self-cleaning and anti-fouling performance, unlike extremely liquid repellent interfaces (*e.g.* superhydrophobic). In this context, the nepenthes pitcher plant-inspired slippery liquid-infused porous surface remained capable of sliding various liquid droplets, but it fails to provide a dry interface; rather unavoidable leaching of the infused liquid lubricant affects its shelf-life.[43–47] To address this challenge, recently solid–slippery interfaces were introduced following a few approaches, *i.e.*, (1) infusion of phase transitioning solid lubricants (polymer and paraffin) in a porous matrix,[48–53] (2) attachment of a flexible polymer,[54–60] (3) growth of polymer brushes,[61–63] (4) layer-by-layer surface growth of nanoparticles[53,64] and deposition of nanoparticles,[65,66] and (5) assembly of oligomers.[67–70] Such earlier reported approaches mainly concentrated on minimizing the nanometric roughness to achieve sliding of beaded droplets of water and organic solvents. Thus, the reports of solid slippery coatings with a comprehensive ability to slide beaded droplets of all types of liquids—including water, polar/non-polar organic solvents, crude oil, commercially available refined and natural oils and even fluorinated liquids are very limited in the relevant literature (Table 1). Moreover, reported solid slippery coatings predominantly suffer from tedious or specific synthesis processes, additional thermal/UV-assisted curing steps, optical transparency, thermal stability, and limited scope for substrate selection, as illustrated in Table 1. Earlier methods were less appropriate to simultaneously and precisely modulate both nanometric roughness and surface free energy. Hence, further

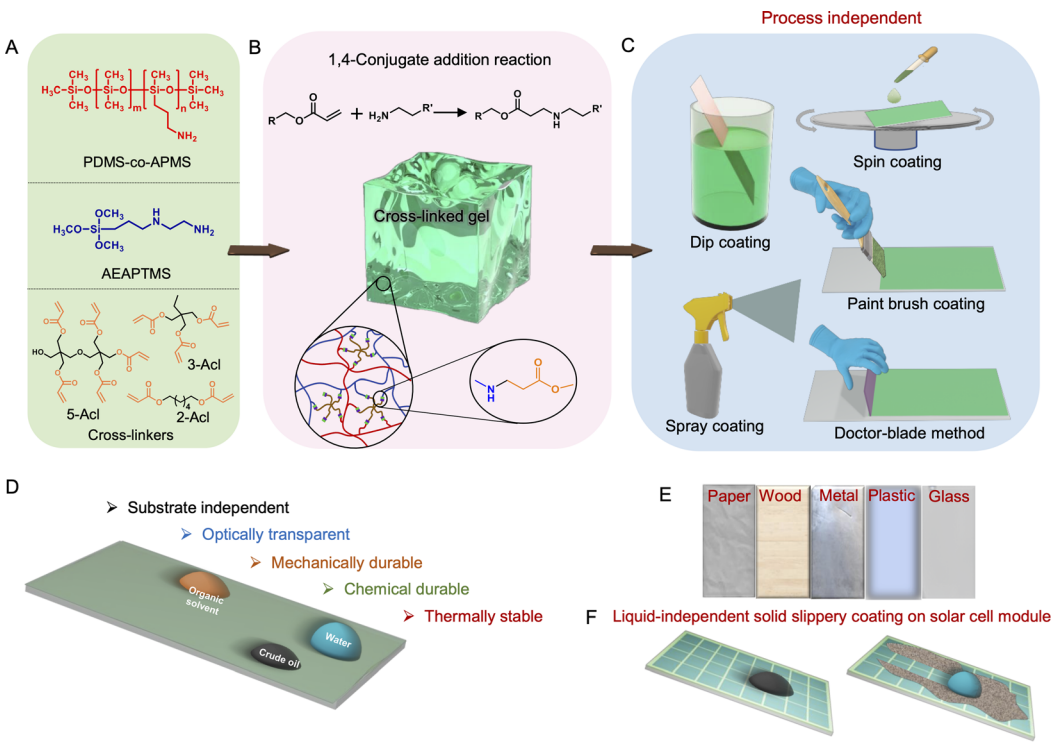

Scheme 1 Design of highly compelling liquid independent solid slippery coating. (A) Chemical structures of 1,6-hexanediol diacrylate (2-Acl), trimethylolpropane triacrylate (3-Acl), dipentaerythritol penta-acrylate (5-Acl), poly[dimethylsiloxane-*co*-(3-aminopropyl)methylsiloxane] (PDMS-*co*-APMS) and 3-(2-aminoethylamino)propyltrimethoxysilane (AEAPTMS). (B) 1,4-Conjugate addition reaction between amine groups of PDMS-*co*-APMS and AEAPTMS and acrylate groups of the selected cross-linker, *i.e.*, 5-Acl, yielded a covalently cross-linked transparent gel through the formation of β-amino ester bonds. (C) Schematic illustration of the preparation of a solid slippery interface utilizing various common approaches—including dip-coating, spin coating, paint-brush, doctor blade and spray deposition. (D and E) Schematic representation of an optically transparent, highly durable liquid independent solid slippery interface on various substrates including paper, wood, metal, plastic and glass. (F) Schematic demonstrating antifouling and self-cleaning of beaded droplets of oil/water and solid particles on a liquid independent solid slippery coated solar cell module.

design of solid slippery coating is essential to address all these relevant and important concerns. Instead of attaching or infusing polymers and growing polymer brushes, here, we report a completely different strategy to develop a highly compelling solid slippery coating, where a covalently cross-linked gelation process is introduced through a 1,4-conjugate addition reaction between selected non-fluorinated three components of a reaction mixture (Scheme 1A–F) under ambient conditions to modulate essential roughness and surface free energy for developing a highly optically transparent (above 95%) and substrate-independent (*e.g.*, paper, wood, metal, plastic, glass *etc.*), process-independent and liquid (polar/nonpolar solvents, and natural, refined and crude oils)-independent tolerant solid slippery coating. The coating was successfully prepared following various commonly adopted methods—including dip-coating, spin coating, paint-brush, doctor blade and spray deposition (Scheme 1C). The covalent cross-linking between selected reactants through β-amino ester bond formation contributed to achieving smooth coating with low surface free energy for conferring liquid-independent solid slippery properties with thermal, mechanical, and chemical stability (Scheme 1D). Taking advantage of high optical transparency and durability, a solar cell module is successfully coated with this prepared solid slippery coating without any perturbation to its photovoltaic performance (Scheme 1F). Moreover, the self-cleaning and anti-fouling ability of this coating protects its performance from deposited dust and oil/oily substances. Thus, this simple chemical approach provided a highly compelling and liquid-independent solid slippery coating that would be useful in various practically relevant applications.

Results and discussion

In the past, 1,4-conjugate addition reaction was extended to develop hierarchically rough coatings to associate heterogeneous liquid wettability.[71–74] In spite of developing rough/porous coating, here, a completely orthogonal strategy is adopted. Covalent crosslinking chemistry is strategically and unprecedentedly introduced to obtain a simple and rapid sol–gel conversion of a reaction mixture of selected primary amine-containing polydimethylsiloxane (poly[dimethylsiloxane-*co*-(3-aminopropyl)methylsiloxane] (PDMS-*co*-APMS)), self-polymerizable monomer (3-(2-aminoethylamino)propyl-trimethoxysilane (AEAPTMS)) and selected crosslinkers (1,6-hexanediol diacrylate (2-Acl), trimethylolpropane triacrylate (3-Acl), and dipentaerythritol penta-acrylate (5-Acl)) through a 1,4-conjugate addition reaction under ambient conditions, as shown in Scheme 1. In this three component-based design of liquid-independent solid slippery coating, AEAPTMS acts as a binder while PDMS-*co*-APMS and the cross-linker synergistically modulate the desired nanometric roughness and low surface energy to confer liquid independent slippery properties. The reaction mixture (RM) of PDMS-*co*-APMS, AEAPTMS and 5-Acl denoted as RM-III produced a transparent gel within 40 minutes, as shown in Fig. 1A, C and S1C† where the molar ratio of 5-Acl, PDMS-*co*-APMS and AEAPTMS was kept at 370 : 2 : 340. In this design, the major constituent (∼61% (w/w)) of the RM-III is the selected crosslinker, *i.e.*, 5-Acl, whereas the weight percentages of other reactants PDMS-*co*-APMS and AEAPTMS are maintained at ∼15% (w/w) and ∼24% (w/w), respectively. The progress of the 1,4-conjugate addition reaction under ambient conditions was monitored with attenuated total reflection-Fourier transform infrared (ATR-FTIR) analysis, where the characteristic IR signatures for the symmetric C–H deformation of the vinyl moiety at 1410 cm^{-1} gradually depleted with respect to the normalized IR signature at 1730 cm^{-1} for carbonyl stretching, as shown in Fig. 1D. This simple IR study unambiguously supported the mutual covalent reaction between selected reactants.

The 1,4-conjugate addition reaction between amine and acrylate resulted in the formation of a β-amino ester bond—where the vinyl moiety is consumed, keeping the carbonyl moiety unaffected (Fig. 1D and S2†). On the other side, a prominent appearance of characteristic IR signatures at 1087 cm^{-1} and 1047 cm^{-1} for antisymmetric stretching vibrations of Si–O–Si was noticed, as shown in Fig. 1D. This simple study validated the self-polymerization of the silane moiety of AEAPTMS. It is worth mentioning that the 1,4-conjugated addition between available amine and acrylate in the reaction mixture resulted in a gradual depletion of the IR signature at 1410 cm^{-1}, whereas IR signatures (at 1087 cm^{-1} and 1047 cm^{-1}) for Si–O–Si linkage because of the self-condensation reaction of selected silane dominated later. Thus, the sol–gel conversion process involves cross-linking through β-amino ester bond formation and the self-polymerization of the silane moiety. In the absence of a cross-linker, the physical state of the transparent reaction mixture of selected reactants remained unaltered and failed to transform into a gel, as shown in Fig. 1B and S1D.† However, for other reaction mixtures, RM-II (reaction mixture-II) and RM-I (reaction mixture-I) having different crosslinkers, *i.e.*, 3-Acl and 2-Acl, provided an opaque gel and a turbid dispersion, respectively, as shown in Fig. 1C, S1A, B and S4.† The choice of cross-linker having the difference in the cross-linking point (*i.e.*, the acrylate group) displayed an obvious influence on the sol–gel conversion process and optical transparency of the resultant gels.

Dynamic light scattering (DLS) study revealed the existence of smaller aggregates in RM-III (∼122 ± 3.8 nm) compared to RM-II (∼377 ± 15.7 nm), prior to their complete sol–gel conversion. RM-II with bigger aggregates appeared more turbid because of more scattering of light. It is worth mentioning that the molar concentration of acrylate functional groups was kept identical for all three different reaction mixtures (RM-I, RM-II, and RM-III)—though different crosslinkers (2-Acl, 3-Acl and 5-Acl) were utilized. The analysis of FTIR spectra of these reaction mixtures after sol–gel conversion revealed the presence of a very similar content of residual acrylate groups (Fig. S3 and S4†), suggesting a similar extent of 1,4-conjugate addition reaction between the available acrylate and amine groups in the respective reaction mixtures. Thereafter, all these reaction mixtures (RM-I, RM-II, and RM-III) were prepared individually—and explored further to prepare liquid independent solid slippery coatings. Thereafter, a series of reaction mixtures

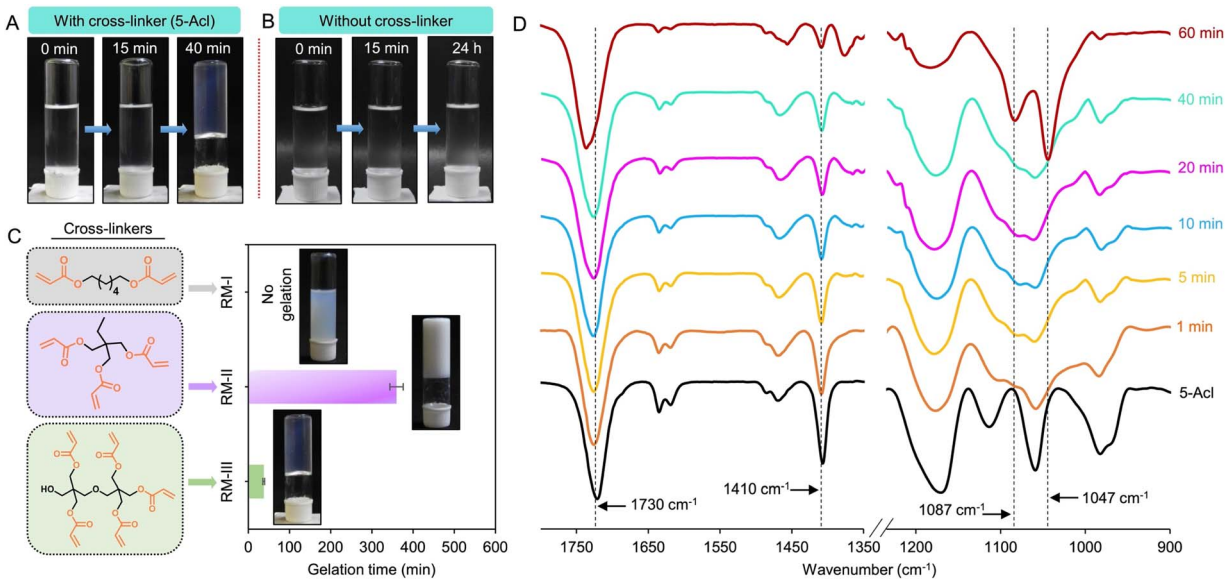

Fig. 1 Optimization of reaction mixtures. (A and B) Digital photographs showing sol–gel conversion of RM-III (where 5-Acl was selected as the cross-linker) resulting in the formation of a transparent gel within 40 min (A), whereas the reaction mixture in the absence of any cross-linker remains unaltered even after keeping it for 1 day (B). (C) Bar graph indicating the time required for conversion of optically transparent different (with respect to selection of crosslinkers: 2-Acl, 3-Acl and 5-Acl) reaction mixtures (RM-I (crosslinker: 2-Acl), RM-II (crosslinker: 3Acl) and RM-III (crosslinker: 5-Acl)) into a gel, where RM-1 failed to form any gel even after 1 day, rather provided a turbid solution. Inset digital images represent the transparent and opaque gels and turbid reaction mixture. (D) Attenuated total reflection-Fourier transform infrared (ATR-FTIR) spectra of RM-III at different time intervals.

(analogues of RM-III) were prepared by mixing primary amine containing reactants (PDMS-*co*-APMS and AEAPTMS) with a selected cross-linker, *i.e.*, 5-Acl in ethanol where the concentration of 5-Acl was altered gradually from 0.07 M to 1.3 M maintaining the concentrations of PDMS-*co*-APMS (0.048 g ml^{-1}) and AEAPTMS (0.07 g ml^{-1}) unperturbed. These reaction mixtures were individually applied on clean glass substrates following the doctor blade method and air-dried under ambient conditions to achieve respective solid and dry coating. Thereafter, both static contact angle (SCA; volume of droplets: 5 μl) and sliding angle (SA) of beaded droplets of water (40 μl) and crude oil (a highly complex organic liquid; 10 μl) on the prepared coatings were examined. The concentration of the selected cross-linker (*i.e.*, 5-Acl) influenced the slippery properties of the resultant coatings. When the concentration of 5-Acl in the deposition solution was maintained in the range of 0.37 M to 0.97 M, the prepared coatings displayed slippery properties for beaded droplets of both water and crude oil with sliding angles of <20° as shown in Fig. 2A.

For example, the coating derived by maintaining the concentration of 5-Acl at 0.37 M enabled the effortless sliding of both beaded droplets of water and oil droplets with a SCA of 105.1° and 31.5° and SA of 17° and 15°, respectively, as shown in Fig. 2B and C. However, for other reaction mixtures having the 5-Acl concentration below and above the mentioned range, the resultant coatings displayed slippery properties only for beaded water droplets at higher sliding angles and absolutely failed to slide beaded droplets of crude oil, as shown in Fig. 2A. To understand this phenomenon, the topography of the three different coatings that were prepared by selecting three distinct concentrations of crosslinker (5-Acl)—*i.e.* 0.07 M, 0.37 M and 1.1 M in RM III, was examined with 3D atomic force microscopy images. A very apparent change in topography for these coatings was noted, as shown Fig. 2D, E and S5.† Moreover, the line profiles presented in Fig. 2F–I and S5† unambiguously indicated the formation of smoother coating on increasing the concentration of the selected crosslinker. The root mean square (RMS) roughness depleted with increasing the concentration of 5-Acl, where RMS roughness values were measured to be ~30 nm, 6 nm and 3 nm for coatings that were derived by maintaining the crosslinker concentration at 0.07 M, 0.37 M and 1.1 M, respectively. Upon further increasing the concentration of crosslinker 5-Acl beyond 1.1 M, the roughness of the coatings remains very similar (Fig. S5 and S6†). The extent of covalent crosslinking is likely to provide a more or less compact polymeric network in the prepared coatings. A denser polymer network is expected to contribute to lowering the surface roughness, and such depletion of surface roughness by the association of crosslinking chemistry has been realized in the past to modulate cell adhesion behavior.[75] But, interestingly, the coatings with the highest and lowest RMS roughness among these selected coatings displayed inability to slide beaded droplets of crude oil as shown in Fig. 2A; rather spillage and spreading of beaded droplets of crude oil were noticed. Thus, the current study unambiguously suggests that surface topography alone is not instrumental in controlling the sliding behaviour of beaded droplets of liquid on a smooth solid interface.

Thereafter, another important parameter, *i.e.*, surface free energy (SFE), of the prepared coating was measured, where the

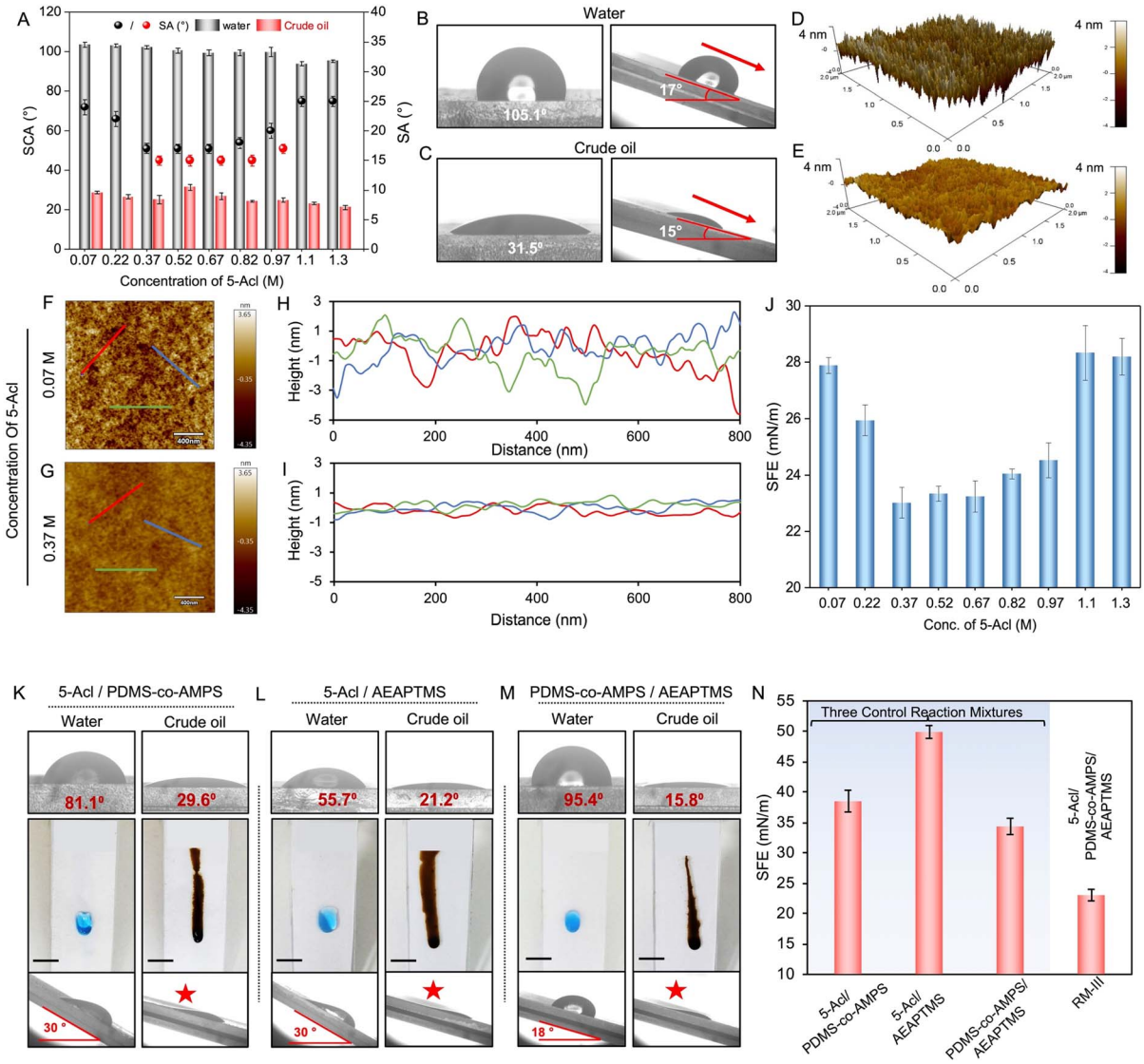

Fig. 2 Crosslinker-assisted simultaneous and precise modulation of roughness and surface free energy. (A) Bar graph depicting the change in static contact angle (SCA) and sliding angle (SA) of beaded droplets of water and crude oil on the coated interface, where the concentration of the selected crosslinker (5-Acl) was gradually increased in reaction mixtures. (B and C) SCA and SA images of beaded droplets of water (B) and crude oil (C) on the optimized (concentration of 5Acl: 0.37 M) coated interface. (D and E) The atomic force microscope (AFM) 3D topography images of coatings obtained with a crosslinker (5-Acl) concentration of 0.07 M (D) and 0.37 M (E) in RM-III. (F–I) Tapping mode 2D topographic AFM images of coatings that were derived maintaining the concentrations of the crosslinker (5-Acl) at 0.07 M (F) and 0.37 M (G) and the corresponding height profiles measured along the red, blue and green lines for coatings with crosslinker (5-Acl) concentrations of 0.07 M (H) and 0.37 M (I). (J) The surface free energy (SFE) of coatings that are derived from different reaction mixtures having only a difference in the concentration of 5-Acl. (K–M) Static contact angle, digital (scale bar: 1 cm) and sliding angle of beaded water and crude oil droplets (5 μl) on 5-Acl/PDMS-*co*-AMPS coated (K), 5-Acl/AEAPTMS coated (L) and PDMS-*co*-AMPS/AEAPTMS coated (M) glass slides. The star mark indicates spilling of crude oil. (N) Bar graph illustrating the surface free energy (SFE) of coatings derived from three different reaction mixtures-5-Acl/PDMS-*co*-AMPS, 5-Acl/AEAPTMS, PDMS-*co*-AMPS/AEAPTMS and RM-III (5-Acl/PDMS-*co*-AMPS/AEAPTMS) where content of acrylate and amine groups was maintained identical.

concentration of the selected crosslinker in RM-III was gradually increased. It was observed that the concentration of the cross-linker influenced the surface free energy of the coating. At lower (below 0.37 M) and higher (above 0.97 M) concentrations of 5-Acl in the depositing reaction mixture, the SFE of the coating was found to be relatively higher in comparison to the selected concentration range (from 0.37 M to 0.97 M), as shown in Fig. 2J. The minimum surface free energy, *i.e.*, 22 mN m^{-1}, was noticed for a 5-Acl concentration of 0.37 M. At lower concentrations of 5-Acl, fewer acrylate groups are available to provide β-amino ester cross-linkages through the 1,4-conjugate addition reaction. Hence, the surface free energy remained high. On increasing the concentration of 5-Acl, more acrylate groups are converted to β-amino ester cross-linkages through the 1,4-conjugate addition reaction, thereby lowering the SFE of the coating, whereas at relatively high concentrations of 5-Acl, the amount of unreacted and residual acrylate groups is more (Fig. S7†), which is again likely to elevate the surface free energy

of the resultant coating. As a consequence, a slight elevation (28 ± 0.88 mN M^{-1} to 30 ± 0.72 mN m^{-1}) in the surface free energy (SFE) of the coating was noticed when increasing the concentration of 5-Acl beyond 1.1 M (Fig. S6†). Thus, β-amino ester cross-linkage in the prepared coating derived from RM-III provided a facile basis to alter surface free energy of a solid coating.

Thereafter, a separate control study was performed to understand the role of β-amino ester cross-linkages in achieving optimum SFE. In this study, three distinct reaction mixtures were prepared by individually mixing crosslinkers with the other two reactants (PDMS-*co*-APMS and AEAPTMS) to develop three different coatings for evaluating their slippery behaviour. First, the selected crosslinker, *i.e.* 5-Acl (0.37 M), was individually mixed with either PDMS-*co*-APMS (2 mM) or AEAPTMS (0.34 M) to get two different reaction mixtures. On the other side, AEAPTMS (0.34 M) and PDMS-*co*-APMS (2 mM) were mixed together to prepare a third reaction mixture. The concentrations of the respective reactants were kept identical to the optimized RM-III that provided the desired slippery behaviour with a low SFE of 22 mN m^{-1}. Interestingly, polymeric coatings derived from these three different reaction mixtures of 5-Acl/PDMS-*co*-APMS, 5-Acl/AEAPTMS and AEAPTMS/PDMS-*co*-APMS failed to display slippery properties against the beaded droplets of crude oil. However, the beaded droplets of water slide at comparatively higher tilting angles, as depicted in Fig. 2K–M. This is because of the comparatively higher (∼35 mN m^{-1} to ∼49 mN m^{-1}) SFE of these three coatings, as shown in Fig. 2N. This controlled study supports that the depletion of SFE of the prepared coating derived from RM-III is not just dependent on the amount of 5-Acl, but rather on the β-amino ester bonds that formed through the mutual reaction between the acrylate group of 5-Acl and amine groups of the other two reactants (PDMS-*co*-APMS or AEAPTMS) attributed to the change in SFE. The content of high β-amino ester bonds in the polymeric coating resulted in a low SFE and allows sliding of both oil and water droplets.

To gradually and orthogonally modulate roughness of coatings—keeping their surface free energy unaltered, another set of control studies was introduced. In this context, separate reaction mixtures were prepared by associating different crosslinkers—i.e., 3-Acl and 2-Acl instead of 5-Acl (RM-III), keeping the content of acrylate groups identical. In addition to RM-III, two different coatings that were derived from these reaction mixtures (RM-I and RM-II) successfully slid both beaded droplets of oil and water, as the SFE of all coatings remained low and very similar (<25 mN m^{-1}, Fig. 3B). However, the sliding angle of the beaded droplets was noticed to be minimum for RM-III (Fig. 3A and S8A–O†). This is likely due to the change in the surface roughness of the resulting coatings. The RMS roughness of the coating derived from RM-III was found to be the least (6 nm), while RM-I provided coating with a relatively higher roughness of 16 nm, as shown in Fig. 3B. Actually, the selected crosslinker having a difference in the crosslinking points (2 acrylate groups in 2-Acl, 3 acrylate groups in 3-Acl and 5 acrylate groups in 5-Acl) is expected to provide polymeric coating with a less or more dense network, as shown in Fig. 3D. Such a difference in the structure (less or more dense) of the polymer network in the prepared coating is likely to control the surface roughness.[75] This study revalidates that (i) low SFE is essential to achieve slippery properties against both water and oil phases and (ii) low roughness improves the sliding angle of beaded liquid droplets on the slippery coating. Thus, both the crosslinking chemistry (*i.e.* β-amino-ester linkage) and the structure of the cross-linked network in the polymeric coating control the slippery properties through controlled modulation of roughness and SFE.

Such a smooth uniform coating remained appropriate to prevent scattering of light and eventually displayed high optical transparency above 95% at a wavelength of 550 nm, as shown in Fig. 3C, where the optical transparency of the coating is normalized with respect to a bare glass substrate. In addition to water and crude oil, the slippery properties of the prepared solid and dry coating were examined against various other liquids, including polar and non-polar organic solvents and refined oils.

The prepared coating remained capable of readily sliding beaded droplets of various types of liquid—including polar (water, DMSO, DMF, glycerol, acetone, hexanol, 1-propanol, methanol, and ethanol), nonpolar (DCE, DIM, toluene, THF, dodecane, and decane) liquids and commercially relevant refined (motor oil, petrol, diesel, and kerosene), crude, and natural (vegetable) oils and fluorinated liquid (Krytox) with a sliding angle well below 20°, as shown in Fig. 3E, S9, S10 and Movie 1,† irrespective of surface tension and viscosity of selected liquids. Thus, the developed coating displayed high optical transparency and liquid independent slippery properties. Interestingly, the simple sol–gel conversion process of the deposited reaction mixture is successfully explored to prepare such anti-fouling interfaces following various standard fabrication methods, including doctor blade, dip coating, paint brush, spray deposition and spin coating without affecting the sliding behavior of beaded droplets of both water and crude oil as shown in Fig. 3F. The deposited solution undergoes a similar sol–gel conversion under ambient conditions, irrespective of the deposition method. Except for air drying under ambient conditions, additional external interventions (*i.e.* heat treatment or UV treatment) are not essential to develop the current coating. The RMS roughness of the prepared coating remained very similar (Fig. S11†)—irrespective of the deposition process, as the depositing solution undergoes the same sol–gel conversion through a 1,4-conjugate addition reaction under ambient conditions.

The durability of the prepared coating against different and severe conditions was examined in detail to check its suitability towards its prospective practical applications under outdoor conditions. In the relevant literature, thermal stability of the solid slippery coating remained a concern; often the earlier reported coating failed to survive temperature beyond 200 °C (Table S1†). In comparison to earlier literature, the prepared coating derived from RM-III displayed superior thermal stability, as its thermal decomposition was noticed only after exposure to temperature beyond 300 °C, as shown in Fig. 4A. The selection of the crosslinker played an important role in tailoring the thermal stability of the prepared coating as is

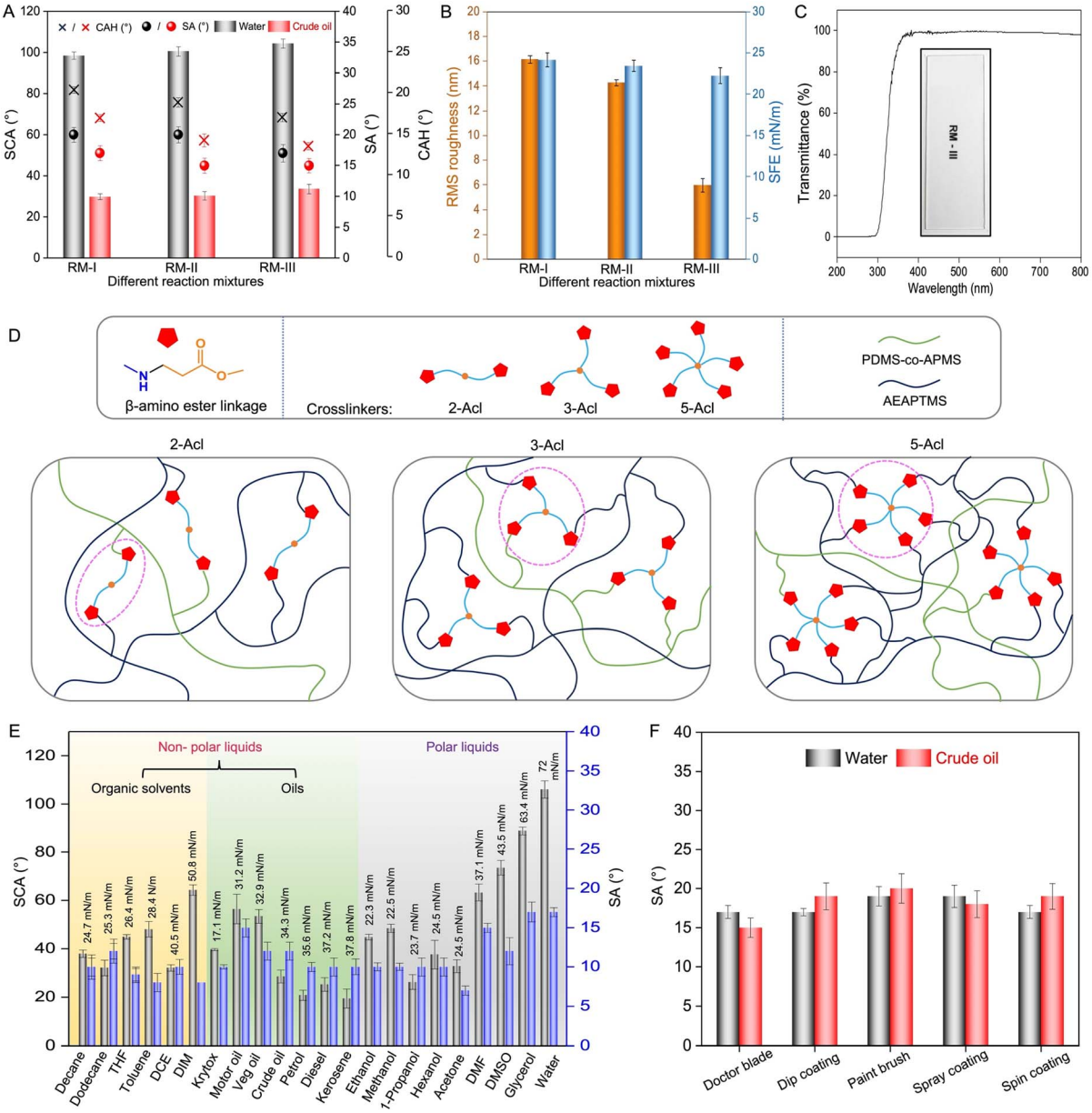

Fig. 3 (A) Comparing the SCA, SA and CAH of water and crude oil droplets on the coated interfaces that are prepared from different reaction mixtures (RM-I, RM-II, and RM-III). (B) The plot illustrating the change in surface roughness (root mean square (RMS) roughness) and surface free energy (SFE) of coatings that are derived from RM-I, RM-II, and RM-III. (C) Presenting the optical transparency of coating prepared from RM-III, normalized with respect to a bare glass substrate. (D) Schematic illustrating the use of different crosslinkers in achieving a denser polymer network. (E) Graph depicting the SCA and SA of various polar/non-polar liquids and refined/crude oils on the coated interface derived from RM-III. (F) The plot depicting the wettability and SA of beaded droplets of water and crude oil on the coatings prepared from RM-III—following different deposition methods.

evident from the early thermal decomposition of the prepared coatings consisting of other crosslinkers, *i.e.*, 3-Acl and 2-Acl, as shown in Fig. 4A. In the absence of cross-linking, the coating derived from a mixture of PDMS-*co*-AMPS and AEAPTMS failed to survive temperatures even below 150 °C. Thus, the appropriate selection of cross-linker in the reaction mixture is attributed to improve the thermal stability of the prepared coating—where the crosslinking density through the β-amino ester bond is likely to play an important role. Importantly, the embedded liquid independent slippery properties of the coating remained unaltered even after thermal exposure of the coating to 300 °C. Both the beaded droplets of water and crude oil readily slide off at a tilting angle of <25°, as shown in Fig. 4B. However, the slippery properties were compromised on exposure to 350 °C due to the thermal decomposition of the prepared coating (Fig. 4B). Apart from this thermal treatment under dry conditions, the prepared coating was also exposed to extremes of temperature under wet conditions, and it survived the treatment with boiling water (100 °C) and cold water (0 °C) and continued to display slippery properties, as shown in

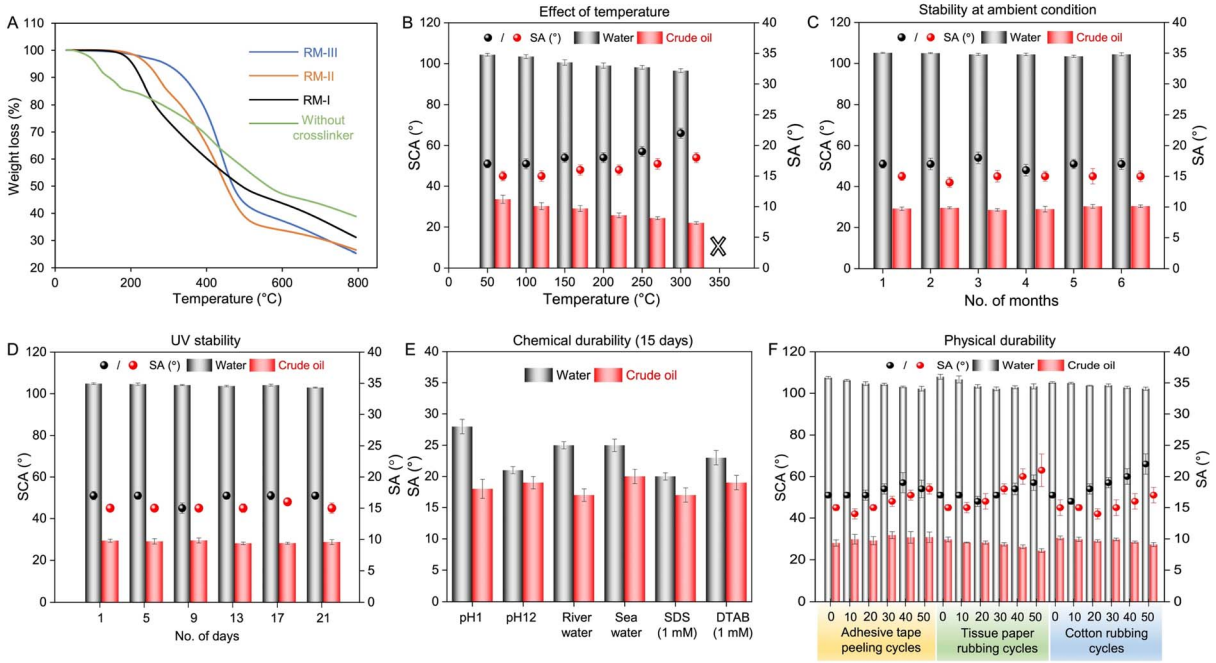

Fig. 4 Durability of liquid independent solid slippery coating. (A) Thermogravimetric analysis of coatings derived from different reaction mixtures without or with selected crosslinkers. (B) Effect of applied temperature on the embedded liquid (water and crude oil) wettability and sliding properties of the prepared coating. (C and D) Stability of the prepared coating under ambient conditions for over 6 months (C) and under UV light exposure (λ_{max} – 365 nm and 254 nm) for three continuous weeks (D). (E) The plot illustrating the chemical durability of the coating at different and challenging aqueous exposures for 15 continuous days. (F) The plot depicting the physical tolerance of the coating under different physically abrasive exposures—including adhesive tape peeling, tissue paper and cotton rubbing tests.

Fig. S12A and B.† Such thermal stability of the coating is attributed to the existence of covalent cross-linkages in the prepared coating.

Next, the stability of the prepared coating under ambient laboratory conditions was examined for over 6 months, where the sliding angles of beaded droplets of water and crude oil were measured after every one month, as shown in Fig. 4C. The slippery properties remained unperturbed over the 6 months. The droplets of water and crude oil beaded with static contact angles (SCAs) of ~105° and ~30°, respectively and readily slid off on titling the prepared coating at ~17° and ~15°. Then, the covalently cross-linked coating was exposed to UV irradiation for 3 weeks and the slippery properties were examined at regular intervals. The beaded crude oil and water droplets readily slid off even after UV light exposure at λ_{max} of 365 nm and 254 nm for 21 days, as shown in Fig. 4D. The prepared coating also displayed tolerance towards different and severe chemical exposures including extremes of pH (1 and 12), river water, artificial seawater, and surfactant contaminated (SDS and DTAB, concentrations of 1 mM) water for prolonged duration (15 days) without perturbing the embedded slippery properties of beaded droplets of water and crude oil, as shown in Fig. 4E.

While the recently reported solid slippery coatings suffered from exposures to extremes of pH and other severe chemicals (Table 1), such a covalently cross-linked approach provided a simple basis to achieve thermal, UV and chemical durability. In addition, the prepared coating also sustained different relevant and widely accepted physical abrasion tests including the adhesive tape peeling test, tissue paper rubbing test and cotton rubbing test for multiple cycles (minimum of 50 times) without compromising the embedded liquid independent solid slippery properties (Fig. 4F and S13A–C†). Importantly, no delamination of the coating was noted during the adhesive tape test, which supports the existence of strong adhesion between the coating and the substrate. In addition, such slippery coatings prepared following different deposition processes using the same reaction mixture (RM-III) displayed a nearly similar durability against the standard adhesive tape peeling test (Fig. S14†). On the other side, the survival of the slippery properties against tissue paper and cotton rubbing tests under an external load of 200 g confirmed the existence of mechanical stability of the prepared coating against relevant physical abrasive exposures. The prepared coating was also tolerant to the sand drop test, where 50 g of sand particles was dropped from a height of 20 cm—however, the prepared coating continued to display slippery properties with effortless sliding of beaded droplets of crude oil and water, as shown in Fig. S15.† Thus, the prepared liquid-independent solid slippery coating with thermal, chemical, and physical durability would be more appropriate for practical applications.

In this section, the anti-fouling, anti-smudge, and self-cleaning performances of the prepared coating were examined in detail. The prepared optically transparent coating was individually and completely submerged in various relevant contaminated aqueous phases (*i.e.*, water, pH 1, pH 12, juice, cola, and muddy water) and commercially available refined

(vegetable oil, motor oil, and kerosene) and crude oils, surfactant (including cationic surfactants (cetyltrimethylammonium bromide (CTAB), 1 mM), anionic surfactants (sodium dodecyl sulfate (SDS), 1 mM) and neutral surfactants (Triton-X 100, 1 mM)) contaminated aqueous phases and crude oil based emulsions (both water-in-crude-oil (2%) and crude-oil-in-water (2%)) as shown in Fig. 5A, S16 and Movie 2.† No trace of liquid was noticed on the prepared coating after removing the coated substrate from the respective liquids. Such self-cleaning performance against a wide range of liquids is attributed to the association of liquid independent slippery properties, unlike the uncoated substrate (Fig. 5B, S16, S17A and B†). Next, commercially available oil and water-based permanent markers were manually applied to write on this coated substrate to demonstrate anti-smudge performance as shown in Fig. 5C. Apparently, an immediate shrinkage of deposited inks was noticed on the coated glass due to the embedded anti-fouling properties. Both oil and water-based deposited inks were easily removed from the coated substrate with the application of gentle tissue paper wiping, as shown in Fig. 5C and Movie 3.† However, a completely different outcome was noticed on repeating the same experiment on a bare glass slide, where the selected oil- and water-based inks deposited more and the rubbing with tissue paper failed to completely wipe out the deposited oil- and water-based inks (Fig. 5D and Movie 3†). This simple study validated the existence of anti-smudge performance of the coating, where both water- and oil-based inks can be readily removed with gentle wiping with tissue paper. Such performance is challenging to achieve with earlier reported solid slippery coatings. The preferred surface free energy, smoothness and covalent cross-linking of the prepared coating together contributed to achieving this superior anti-smudge performance.

Thereafter, the prepared coating was explored in demonstrating the self-cleaning of deposited relevant solid particulates having different size distributions (Fig. S18A–C†) including dust, sand and fly ash, and the self-cleaning performance was compared with that of a bio-inspired

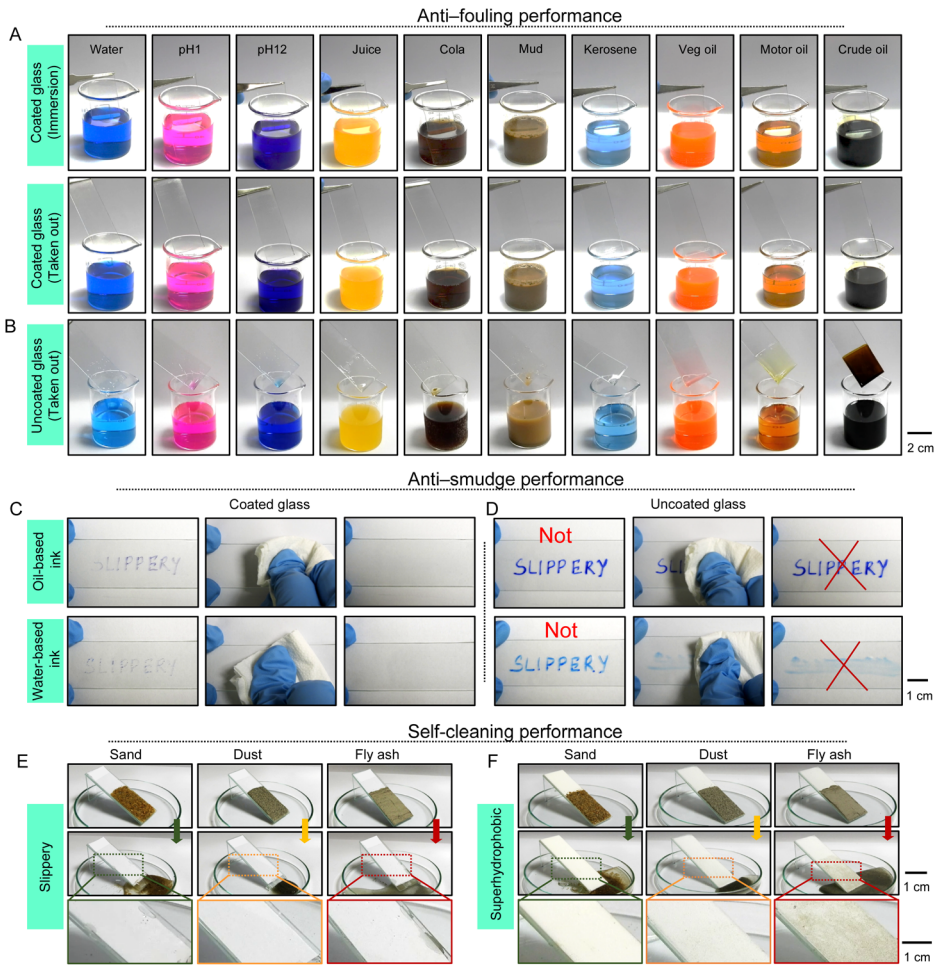

Fig. 5 Anti-fouling, anti-smudge, and self-cleaning properties of the prepared coating. (A and B) Digital photographs of the coated (A) and uncoated (B) interface after immersion and taking out of different aqueous phases and oils. (C and D) Sequential digital photographs depicting the anti-smudge performance of coated (C) and uncoated (D) glass, where both oil- and water-based inks were deposited prior to being wiped out with tissue paper. (E and F) Photographs comparing the self-cleaning of deposited sand, dust, and fly ash particulates on coated slippery (E) and superhydrophobic (F) interfaces.

superhydrophobic coating which is well-recognized for its self-cleaning ability. The prepared liquid independent solid slippery coating displayed absolute self-cleaning ability towards selected solid particles. During the sliding of aqueous droplets on the prepared slippery coating, the deposited solid particles were removed away from the interface to providing an instantly clean and dry interface, as shown in Fig. 5E and Movie 4.† However, the superhydrophobic coating that consisted of hierarchically rough topography failed to completely clean the fine dust particles and fly ash, as shown in Fig. 5F and Movie 5.† Only the deposited sand particles having comparatively large particle sizes (Fig. S18A†) were self-cleaned on the superhydrophobic interface. As expected, the fine solid particles (particularly fly ash and dust particles; Fig. 5F and S18B and C†) accumulated in the grooves of the rough topography of the superhydrophobic coating and thus suffered from the incomplete cleaning of the superhydrophobic interface. But the prepared solid slippery coating having an ultra-smooth feature prevented such accumulation of solid particulates and displayed a superior self-cleaning performance (Fig. 5E).

Taking advantage of the self-cleaning ability and high optical transparency of the prepared coating, we have demonstrated the potential application of this coating on commercially available solar cell modules to keep its performance unperturbed in outdoor settings. The solid slippery coating (SCA = 105.6° and SA = 17° for water and SCA = 55.5° and SA = 16° for vegetable oil; Fig. S19A and B†) was applied on a solar cell module to achieve (a) effortless sliding of the beaded droplets of oil and water (Fig. 6A and S19B†) and (b) self-cleaning of the different deposited solid particulates, as shown in Fig. 6A. As expected, the uncoated solar cell module absolutely failed to (i) slide beaded droplets of water and oil and (ii) self-clean the deposited dust under a similar experimental set-up (Fig. 6B, S19C and D†). More importantly, the deposition of this solid slippery coating on the solar cell module barely affects the photovoltaic performance (Fig. 6C) as it displays high optical transparency in the visible light spectrum. Thereafter, the coated solar cell module and uncoated solar cell module were individually and consecutively exposed to oil droplets (vegetable oil) and dust particles prior to water exposure (Fig. 6A and B). This entire experiment was repeated for 50 cycles, and the output power of the coated and uncoated solar cell modules was measured after every 10 cycles, as shown in Fig. 6D. We noticed a gradual loss of performance of the uncoated solar cell module with increasing self-cleaning cycles due to incomplete removal of oil and dust particles, whereas the coated solar cell module remained successful in keeping the output power unperturbed over the entire 50 cycles under an identical experimental set-up due to its self-cleaning ability. Thus, the prepared coating provided a more appropriate remedy to protect the performance of solar panels from the unavoidable challenges of deposited dust, dirt, and other organic and oily substances.

Next, the optically transparent liquid independent solid slippery coating was successfully applied on other commercially relevant substrates including wrist watch covers and spectacles, where the right half of the selected substrates was coated with slippery coating and the left half was kept uncoated to compare

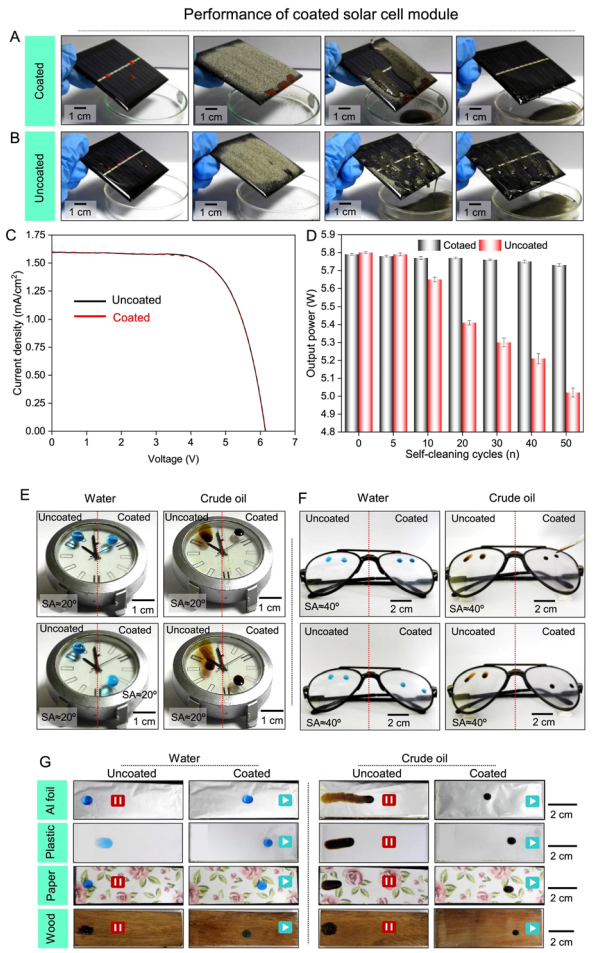

Fig. 6 Impact of the prepared liquid independent solid slippery coating on different substrates. (A and B) Self-cleaning demonstration of deposited dust particulates on coated (A) and uncoated (B) solar cell modules. (C) Photovoltaic performance study of coated and uncoated solar cell modules. (D) The changes in output power of the coated and uncoated solar cell modules during repetitive self-cleaning demonstration 50 times. (E and F) Photographs depicting the sliding of beaded water and crude oil droplets on the coated region (right side of the red color dotted line) of the wrist watch cover (E) and spectacles (F), whereas the uncoated region (left side of the red color dotted line) of the wrist watch cover (sliding angle ~20°); (E) and spectacles (sliding angle ~40°); (F) the pinning and spreading of water and crude oil droplets, respectively. (G) Photographs showing the sliding of water and crude oil droplets on the coated aluminium foil (Al foil), plastic, paper, and wood, whereas on the uncoated substrate, water and crude oil droplets pinned and readily spread, respectively. (The red color 'pause' sign indicates pinning and spreading of beaded liquid droplets on the uncoated substrate, whereas the green color 'play' sign refers to the effortless sliding of beaded droplets of water and crude oil).

the wettability and sliding behavior of beaded droplets of water and crude oil. As expected, the coated area of the substrate readily slides off the beaded droplets of both water and crude oil without leaving any trace of beaded liquid, whereas the droplets of water and oil strongly adhered and spilled, respectively, on the uncoated portion of the selected substrate as shown in Fig. 6E and F. Importantly, such coating can be successfully applied to many other relevant substrates—including metal,

plastic, paper, and wood. On application of the prepared liquid independent coating, all the mentioned oleophilic and hydrophilic substrates (Fig. S20A and B†) became capable of sliding beaded droplets of both water and crude oil, while the uncoated substrate failed to display such anti-fouling properties (Fig. 6G). Additionally, atomic force microscopy (AFM) analysis revealed the presence of similar roughness for different coated substrates, as shown in Fig. S21.† As a consequence, deposited coatings on various substrates displayed very similar slippery properties. The strategically selected 3-(2-aminoethylamino) propyltrimethoxysilane (AEAPTMS) present in the reaction mixture acts as a binding agent and significantly contributes to the adhesive interaction between the coating and underlying substrates. We have investigated the mechanical durability of this developed coating on different substrates where no delamination of the coating was observed after the adhesive tape peeling test and it remained effective in repelling both water and crude oil as shown in Fig. S22.† Thus, the current chemical approach provided substrate-independent, process-independent, optically transparent, and mechanically, chemically, and thermally durable liquid independent solid slippery coating.

Conclusions

While an extremely water-repellent hierarchically rough coating and a liquid-infused slippery porous surface generally suffered from incomplete self-cleaning of ultra-fine particulates and poor shelf-life, respectively, we successfully developed a non-fluorinated liquid-independent solid slippery coating through precise and simultaneous modulation of nanometric roughness and surface free energy. This current covalent crosslinking-based approach aims to design a more comprehensive solid slippery coating that is embedded with various other relevant properties—including high optical transparency, chemical, thermal, and mechanical stability. Moreover, the prepared coating was successfully applied on various types of substrates (glass, plastic, paper, wood, and metal) following commonly and widely accepted different deposition processes (doctor blade method, dip-coating, spray coating, spin coating, *etc*). In our current design, the 1,4-conjugate addition reaction between three selected reactants (polydimethylsiloxane (poly[dimethylsiloxane-*co*-(3-aminopropyl) methylsiloxane] (PDMS-*co*-APMS), 3-(2-aminoethylamino)propyltrimethoxysilane (AEAPTMS) and dipentaerythritol penta-acrylate (5-Acl)) yielded a gel, where the β-amino-ester bond provided the essential low surface energy to display effortless sliding of beaded droplets of water, polar/nonpolar organic solvents, crude, and refined oils. Moreover, the selection of an appropriate crosslinker improved the thermal stability of the coating from 190 °C to 310 °C. The prepared coating remained appropriate to survive prolonged exposures (15 days) to extremes of pH (1 and 12), seawater and surfactant-contaminated aqueous phases. It remained tolerant to commonly adopted physical abrasion tests including adhesive tape peeling, cotton wiping, tissue paper wiping tests and sand drop test. More importantly, such durable coating that displayed superior anti-smudge, anti-fouling and self-cleaning abilities was successfully applied to a commercially available solar cell module without compromising its photovoltaic performance. The liquid independent solid slippery coating remained efficient in self-cleaning beaded oil-droplets and solid particulates to display unaltered photovoltaic performance of the coated solar cell module even after repetitive exposures to oil and dust. Although the sliding angle of beaded liquids on the prepared coating is relatively higher than that of the earlier reported liquid like or semisolid slippery coating, the prepared liquid-independent solid slippery coating with all-inclusive features would be appropriate for various other potential applications—including underwater gas transport.[76,77] In addition to sliding various beaded liquids in air, this chemical approach of controlled modulation of topography and surface free energy is likely to provide a facile basis for precisely modulating both air-bubble wettability and adhesion. Thus, the current approach has the ability for controlled underwater gas delivery, gas sensing, efficient water splitting *etc.*

Data availability

The data that support the findings of this study are available upon reasonable request from corresponding author.

Author contributions

DS and MD: investigation, methodology, data collection, data analysis, validation, and writing & review; AD: methodology, review and editing; SM: data collection, review and editing; AP: data collection and review; UM: supervision, conceptualization, methodology, writing and funding acquisition.

Conflicts of interest

The authors declare no conflict of interest.

Acknowledgements

We thank the Science and Engineering Research Board (CRG/2022/000710), Ministry of Electronics and Information Technology (no. 5(1)/2022-NANO) and DBT (BT/PR45283/NER/95/1919/2022) for financial support. Generous support from DST (DST-FIST programme; Sanction no. SR/FST/CS-II/2017/23C) is acknowledged with appreciation. We are thankful to CIF, CFN, SHST and the Department of Chemistry, Indian Institute of Technology-Guwahati. We thank Prof. P. K. Iyer and Mr Himangshu Baishya for their generous support in photovoltaic measurements of commercially available solar cell modules. MD thanks the institute and MoE for her PhD fellowship. DS thanks UGC for her JRF fellowship.

References

1 S. Chu, Y. Cui and N. Liu, *Nat. Mater.*, 2017, **16**, 16–22.
2 S. Chu and A. Majumdar, *Nature*, 2012, **488**, 294–303.
3 P. Bajpai and V. Dash, *Renewable Sustainable Energy Rev.*, 2012, **16**, 2926–2939.

4 N. Armaroli and V. Balzani, *Angew. Chem., Int. Ed.*, 2007, **46**, 52–66.
5 S. G. Al-Ghamdi and M. M. Bilec, *Environ. Sci. Technol.*, 2016, **50**, 4606–4614.
6 R. Eisenberg and D. G. Nocera, *Inorg. Chem.*, 2005, **44**, 6799–6801.
7 K. Matuszek, M. Kar, J. M. Pringle and D. R. MacFarlane, *Chem. Rev.*, 2023, **123**, 491–514.
8 L. A. Weinstein, J. Loomis, B. Bhatia, D. M. Bierman, E. N. Wang and G. Chen, *Chem. Rev.*, 2015, **115**, 12797–12838.
9 N. Kannan and D. Vakeesan, *Renewable Sustainable Energy Rev.*, 2016, **62**, 1092–1105.
10 N. S. Lewis, *Science*, 2016, **351**, 353.
11 D. Kraemer, B. Poudel, H.-P. Feng, J. C. Caylor, B. Yu, X. Yan, Y. Ma, X. Wang, D. Wang, A. Muto, K. McEnaney, M. Chiesa, Z. Ren and G. Chen, *Nat. Mater.*, 2011, **10**, 532–538.
12 K. Ilse, L. Micheli, B. W. Figgis, K. Lange, D. Daßler, H. Hanifi, F. Wolfertstetter, V. Naumann, C. Hagendorf, R. Gottschalg and J. Bagdahn, *Joule*, 2019, **3**, 2303–2321.
13 B. O. Olorunfemi, O. A. Ogbolumani and N. Nwulu, *Sustainability*, 2022, **14**, 10920.
14 M. J. Adinoyi and S. A. M. Said, *Renewable Energy*, 2013, **60**, 633–636.
15 M. R. Maghami, H. Hizam, C. Gomes, M. A. Radzi, M. I. Rezadad and S. Hajighorbani, *Renewable Sustainable Energy Rev.*, 2016, **59**, 1307–1316.
16 T. Sarver, A. Al-Qaraghuli and L. L. Kazmerski, *Renewable Sustainable Energy Rev.*, 2013, **22**, 698–733.
17 M. Valerino, A. Ratnaparkhi, C. Ghoroi and M. Bergin, *Sol. Energy*, 2021, **227**, 44–55.
18 B. S. Yilbas, H. Ali, M. M. Khaled, N. Al-Aqeeli, N. Abu-Dheir and K. K. Varanasi, *Sci. Rep.*, 2015, **5**, 15833.
19 S. Panat and K. K. Varanasi, *Sci. Adv.*, 2022, **8**, eabm0078.
20 T. Salamah, A. Ramahi, K. Alamara, A. Juaidi, R. Abdallah, M. A. Abdelkareema, E.-C. Amer and A. G. Olabi, *Sci. Total Environ.*, 2022, **827**, 154050.
21 B. O. Olorunfemi, O. A. Ogbolumani and N. Nwulu, *Sustainability*, 2022, **14**, 10920.
22 B. O. Olorunfemi, N. I. Nwulu and O. A. Ogbolumani, *MethodsX*, 2023, **10**, 101967.
23 M. K. Smith, C. C. Wamser, K. E. James, S. Moody, D. J. Sailor and T. N. Rosenstiel, *J. Sol. Energy Eng.*, 2013, **135**, 034505.
24 S. Das, A. Das, D. Parbat and U. Manna, *ACS Appl. Mater. Interfaces*, 2019, **11**, 34316–34329.
25 H. Zhu, S. Cai, G. Liao, Z. F. Gao, X. Min, Y. Huang, S. Jin and F. Xia, *ACS Catal.*, 2021, **11**, 14751–14771.
26 K. M. Wisdom, J. A. Watson, X. Qua, F. Liu, G. S. Watson and C. H. Chen, *Proc. Natl. Acad. Sci. U.S.A.*, 2013, **110**, 7992–7997.
27 X. Zhang, Z. Li, K. Liu and L. Jiang, *Adv. Funct. Mater.*, 2013, **23**, 2881–2886.
28 M. Dhar, A. Das, A. Shome, A. Borbora and U. Manna, *Mater. Horiz.*, 2021, **8**, 2717–2725.
29 P. Papadopoulos, L. Mammen, X. Deng, D. Vollmer and H.-J. Butt, *Proc. Natl. Acad. Sci. U.S.A.*, 2013, **110**, 3254–3258.
30 H. Lambleya, T. M. Schutziusa and D. Poulikakos, *Proc. Natl. Acad. Sci. U.S.A.*, 2020, **117**, 27188–27194.
31 X. Tian, T. Verho and R. H. A. Ras, *Science*, 2016, **352**, 142–143.
32 T.-S. Wong, S. H. Kang, S. K. Y. Tang, E. J. Smythe, B. D. Hatton, A. Grinthal and J. Aizenberg, *Nature*, 2011, **477**, 443–447.
33 F. Geyer, M. D'Acunzi, A. Sharifi-Aghili, A. Saal, N. Gao, A. Kaltbeitzel, T. F. Sloot, R. Berger, H.-J. Butt and D. Vollmer, *Sci. Adv.*, 2020, **6**, eaaw9727.
34 A. Das and U. Manna, *Nanoscale*, 2020, **12**, 24349–24356.
35 W. S. Y. Wong, T. P. Corrales, A. Naga, P. Baumli, A. Kaltbeitzel, M. Kappl, P. Papadopoulos, D. Vollmer and H.-J. Butt, *ACS Nano*, 2020, **14**, 3836–3846.
36 Z. Chu and S. Seeger, *Chem. Soc. Rev.*, 2014, **43**, 2784–2798.
37 Y. Sun and Z. Guo, *Nanoscale Horiz.*, 2019, **4**, 52–76.
38 T. Wang, C. Lv, L. Ji, X. He and S. Wang, *ACS Appl. Mater. Interfaces*, 2020, **12**, 49155–49164.
39 X. Li, D. Wang, Y. Tan, J. Yang and X. Deng, *ACS Appl. Mater. Interfaces*, 2019, **11**, 29458–29465.
40 X. Zhou, J. Liu, W. Liu, W. Steffen and H.-J. Butt, *Adv. Mater.*, 2022, **34**, 2107901.
41 C. Yan, P. Jiang, X. Jia and X. Wang, *Nanoscale*, 2020, **12**, 2924–2938.
42 M. Yu, S. Chen, B. Zhang, D. Qiu and S. Cui, *Langmuir*, 2014, **30**, 13615–13621.
43 S. Peppou-Chapman, J. K. Hong, A. Waterhouse and C. Neto, *Chem. Soc. Rev.*, 2020, **49**, 3688–3715.
44 X. Chen, G. Wen and Z. Guo, *Mater. Horiz.*, 2020, **7**, 1697–1726.
45 J. S. Wexler, I. Jacobi and H. A. Stone, *Phys. Rev. Lett.*, 2015, **114**, 168301.
46 S. Peppou-Chapman and C. Neto, *Langmuir*, 2021, **37**, 3025–3037.
47 C. Vega-Sánchez and C. Neto, *Langmuir*, 2022, **38**, 10568–10574.
48 M. Dhar, A. Das, D. Parbat and U. Manna, *Angew. Chem., Int. Ed.*, 2022, **134**, e202116763.
49 G. Han, T.-B. Nguyen, S. Park, Y. Jung, J. Lee and H. Lim, *ACS Nano*, 2020, **14**, 10198–10209.
50 F. Wang, M. Liu, C. Liu, Q. Zhao, T. Wang, Z. Wang and X. Du, *Sci. Adv.*, 2022, **8**, eabp9369.
51 X. Meng, Z. Wang, L. Wang, L. Heng and L. Jiang, *J. Mater. Chem. A*, 2018, **6**, 16355–16360.
52 K. Han, Z. Wang, L. Heng and L. Jiang, *J. Mater. Chem. A*, 2021, **9**, 16974–16981.
53 W. Niu, G. Y. Chen, H. Xu, X. Liu and J. Sun, *Adv. Mater.*, 2022, **34**, 2108232.
54 W. S. Y. Wong, A. Naga, L. Hauer, P. Baumli, H. Bauer, K. I. Hegner, M. D'Acunzi, A. Kaltbeitzel, H.-J. Butt and D. Vollmer, *Nat. Commun.*, 2021, **12**, 5358.
55 L. Wang and T. J. McCarthy, *Angew. Chem., Int. Ed.*, 2016, **55**, 244–248.
56 L. Xie, X. Cui, J. Liu, Q. Lu, J. Huang, X. Mao, D. Yang, J. Tan, H. Zhang and H. Zeng, *ACS Appl. Mater. Interfaces*, 2021, **13**, 6941–6950.

57 A. B. Tesler, L. H. Prado, M. M. Khusniyarov, I. Thievessen, A. Mazare, L. Fischer, S. Virtanen, W. H. Goldmann and P. Schmuki, *Adv. Funct. Mater.*, 2021, **31**, 2101090.
58 X. Mao, J. Tan, L. Xie, J. Wang and H. Zeng, *Chem. Eng. J.*, 2021, **404**, 127064.
59 H. Zhao, C. A. Deshpande, L. Li, X. Yan, M. J. Hoque, G. Kuntumalla, M. C. Rajagopal, H. C. Chang, Y. Meng, S. Sundar, P. Ferreira, C. Shao, S. Salapaka, S. Sinha and N. Miljkovic, *ACS Appl. Mater. Interfaces*, 2020, **12**, 12054–12067.
60 L. Zhang, Z. Guo, J. Sarma and X. Dai, *ACS Appl. Mater. Interfaces*, 2020, **12**, 20084–20095.
61 J. Liu, Y. Sun, X. Zhou, X. Li, M. Kappl, W. Steffen and H.-J. Butt, *Adv. Mater.*, 2021, **33**, 2100237.
62 M. Rabnawaz and G. Liu, *Angew. Chem., Int. Ed.*, 2015, **54**, 6516–6520.
63 P. Liu, H. Zhang, W. He, H. Li, J. Jiang, M. Liu, H. Sun, M. He, J. Cui, L. Jiang and X. Yao, *ACS Nano*, 2017, **11**, 2248–2256.
64 V. Singh, X. Men and M. K. Tiwari, *Nano Lett.*, 2021, **21**, 3480–3486.
65 W. Pan, Q. Wang, J. Ma, W. Xu, J. Sun, X. Liu and J. Song, *Adv. Funct. Mater.*, 2023, **33**, 2302311.
66 S. Kumar, M. Dhar, B. M. Prusty, D. Sarkar, A. Das, D. Manna and U. Manna, *Chem. Eng. J.*, 2023, **465**, 142776.
67 K. Zhang, S. Huang, J. Wang and G. Liu, *Angew. Chem., Int. Ed.*, 2019, **58**, 12132–12137.
68 M. Liu, Z. Wang, P. Liu, Z. Wang, H. Yao and X. Yao, *Sci. Adv.*, 2019, **5**, eaaw5643.
69 W. Zheng, J. Huang, X. Zang, X. Xu, W. Cai, Z. Lin and Y. Lai, *Adv. Mater.*, 2022, **34**, 2204581.
70 S. Huang, G. Liu, H. Hu, J. Wang, K. Zhang and J. Buddingh, *Chem. Eng. J.*, 2018, **351**, 210–220.
71 A. Shome, A. Das and U. Manna, *Chem. Mater.*, 2021, **33**, 8941–8959.
72 S. L. Bechler and D. M. Lynn, *Biomacromolecules*, 2012, **13**, 1523–1532.
73 M. Dhar, U. I. Kara, S. Das, Y. Xu, S. Mandal, R. L. Dupont, E. C. Boerner, B. Chen, Y. Yao, X. Wang and U. Manna, *Mater. Horiz.*, 2023, **10**, 2204–2214.
74 J. Ford, S. R. Marder and S. Yang, *Chem. Mater.*, 2009, **21**, 476–483.
75 C. N. Grover, J. H. Gwynne, N. Pugh, S. Hamaia, R. W. Farndale, S. M. Best and R. E. Cameron, *Acta Biomater.*, 2012, **8**, 3080–3090.
76 X. Wang, H. Bai, Z. Li, Y. Tian, T. Zhaoa and M. Cao, *Mater. Horiz.*, 2023, **10**, 3351–3359.
77 X. Wang, H. Bai, J. Yang, Z. Li, Y. Wu, C. Yu, L. Jiang and M. Cao, *Small*, 2021, **17**, 2007803.